View metadata, citation and similar papers at core.ac.uk

brought to you by CORE

provided by AIR Universita degli studi di Milano

inorganics

MDPI

Article

Adsorption Properties of $Ce_5(BDC)_{7.5}(DMF)_4$ MOF

Cesare Atzori [1], Jayashree Ethiraj [2], Valentina Colombo [3], Francesca Bonino [1,*] and Silvia Bordiga [1]

[1] Department of Chemistry, NIS and INSTM Reference Centre, Università di Torino, Via G. Quarello 15, I-10135 and Via P. Giuria 7, I-10125 Torino, Italy; cesare.atzori@unito.it (C.A.); silvia.bordiga@unito.it (S.B.)

[2] National Centre for Catalysis Research and Department of Chemistry, Indian Institute of Technology Madras, Chennai 60036, India; jaijoy18@gmail.com

[3] Department of Chemistry, Università degli Studi di Milano, Via C. Golgi 19, I-20133 Milano, Italy; valentina.colombo@unimi.it

* Correspondence: francesca.bonino@unito.it

Received: 7 November 2019; Accepted: 21 January 2020; Published: 26 January 2020

Abstract: In this article we report on the spectroscopic and adsorptive studies done on Ce(III)-based MOF possessing, upon desolvation, open metal sites, and a discrete surface area. The Ce-based MOF was synthesized from terephthalic acid linker (H_2BDC) and Ce^{3+} cations by the classical solvothermal method. Preliminary powder X-ray diffraction analysis showed that the obtained materials corresponded to the ones reported by other authors. Spectroscopic techniques, such as XAS and in situ FTIR with probe molecules were used. In situ FTIR spectroscopy confirmed the successful removal of DMF molecules within the pore system at temperatures above 250 °C. Moreover, the use of CO as a probe molecule evidenced the presence of a Ce^{3+} open metal sites. Detailed volumetric and calorimetric CO_2 adsorption studies are also reported.

Keywords: cerium; MOF; terephthalic acid; spectroscopic characterization; adsorption; calorimetry; carbon dioxide

1. Introduction

Cerium is the most abundant lanthanide element present in the earth crust [1,2] and the ores that are mined for the extraction of more rare and precious rare earth elements (REEs) are also rich in Ce; thus, its cost is relatively low. Its oxide, CeO_2, commonly named ceria, is particularly relevant for redox chemistry, being a catalyst for oxidation and reduction reactions [3], for example, combustion catalysis [4] and photocatalysis [3].

Ce-based MOFs have recently created interest in the scientific community. General features that can be drawn from looking at the current published literature are the following: (i) both Ce^{3+} and Ce^{4+} oxidation states can be used in the synthesis of MOFs [5–9]; (ii) synthetic conditions for Ce^{3+}-containing MOFs tends to be harsher than Ce^{4+} [5,6,10]; (iii) usually, Ce^{4+} starting reagents may be reduced to Ce^{3+} during the synthesis [11,12]; (iv) Ce^{3+} materials more frequently have peculiar structures, while Ce^{4+} tends to give rise to MOFs with the same structure as other 4+ cations (e.g., Zr^{4+} or Hf^{4+}) [5–7,13,14]. Their thermal stability is generally lower than their Zr^{4+} counterparts [7,8,14,15]. As a possible application of Ce MOFs as redox catalysts, Smolders et al. [8] reported the successful use of Ce^{4+}-UiO-67 in the aerobic oxidation of benzylic alcohol to benzaldehyde mediated by TEMPO (2,2,6,6-Tetramethylpiperidinyloxyl). Furthermore, Ethiraj et al. [5] reported the use of a Ce^{3+}-based MOF for the selective capture and storage of CO_2, obtaining high figures of merit of capacity and separation.

The present work reports on the synthesis, spectroscopic characterization, and adsorption properties of Ce^{3+}-based MOFs with terephthalic acid (H_2BDC) as the linker. This material has been already introduced in the literature by D'Arras et al. [11], who discovered it and suggested its crystal

structure in the as-synthesized form, together with the characterization of the thermal properties. However, the porosity of the material has not been studied, indeed, here we report on its adsorption properties, examined through spectroscopic techniques (XAS and in situ FTIR) and adsorption isotherms.

2. Results and Discussion

$Ce_5(BDC)_{7.5}(DMF)_4$ MOF [16] optimized synthesis is reported in the Supplementary Materials. The $Ce_5(BDC)_{7.5}(DMF)_4$ PXRD pattern was coincident with the one reported by D'Arras et al. [11]. The hypothesized structure was taken from Reference [11] and it is reported in Figure 1, for clarity. The asymmetric unit of crystalline structure shows chains of five independent cerium atoms arranged linearly and surrounded by BDC^{2-} and DMF molecules (see Figure 1a). The two terminal atoms of the group are coordinated by eight oxygen atoms in a distorted square antiprismatic shape: six oxygen atoms belong to BDC^{2-} and two oxygen atoms to DMF molecules, while the "central" three cerium atoms are coordinated with nine oxygens, all coming from the ligands, in an uncommon distorted shape. There are mono-dimensional or 1D channels formed in the structure parallel to the Ce chains along the crystallographic $1\bar{1}0$ direction. As depicted in Figure 1b, these micropores are mainly occupied by the coordinated DMF molecules, which protrude into the pores. The surface area and porosity of the material were clarified by the N_2 adsorption experiments (vide infra).

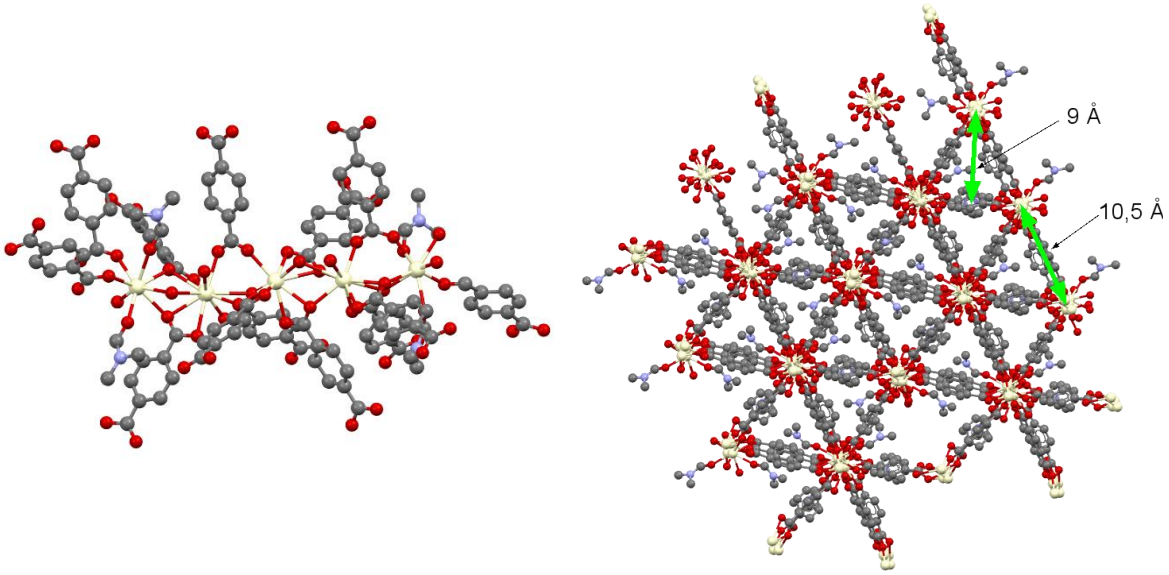

Figure 1. Structure of $Ce_5(BDC)_{7.5}(DMF)_4$. (**a**) Depiction of the asymmetric unit, containing five Ce atoms, 18 BDC^{2-}, and four DMF molecules. Cerium, carbon, nitrogen, and oxygen atoms are pale yellow, black, blue, and red respectively; hydrogen atoms are omitted for the sake of clarity; (**b**) a view through the $1\bar{1}0$ direction. Meaningful distances are highlighted.

The powder diffraction pattern of the as synthesized material, as shown in the synthesis development reported in the Supplementary Materials (Figures S1–S3), was compared to the calculated powder pattern obtained from the crystal structure reported by D'Arras et al. (Figure S3). SEM images of the synthesized powder are available in Figure S4.

A variable temperature powder X-ray diffraction (VTXRD) experiment in N_2 flow in the RT–600 °C temperature range (see Figure 2) showed that the material maintained the crystallinity until 475 °C, undergoing some changes in the XRD pattern, especially from 200 to 250 °C (highlighted in blue color), which could be due to the solvent removal, as strongly suggested by the TGA measurements reported in Figure S5.

The solution of the crystal structure of the desolvated material was out of the scope of the present work. At 500 °C the MOF started decomposing and at 525 °C the formation of broad diffraction peaks

due to cerium dioxide was visible. The broadness of the peaks testifies that the particles were nanometric in size. Scherrer's equation [3], corrected by instrumental broadening using a Si standard from NIST, suggested a size for the cerium dioxide particles of 5 ± 1 nm.

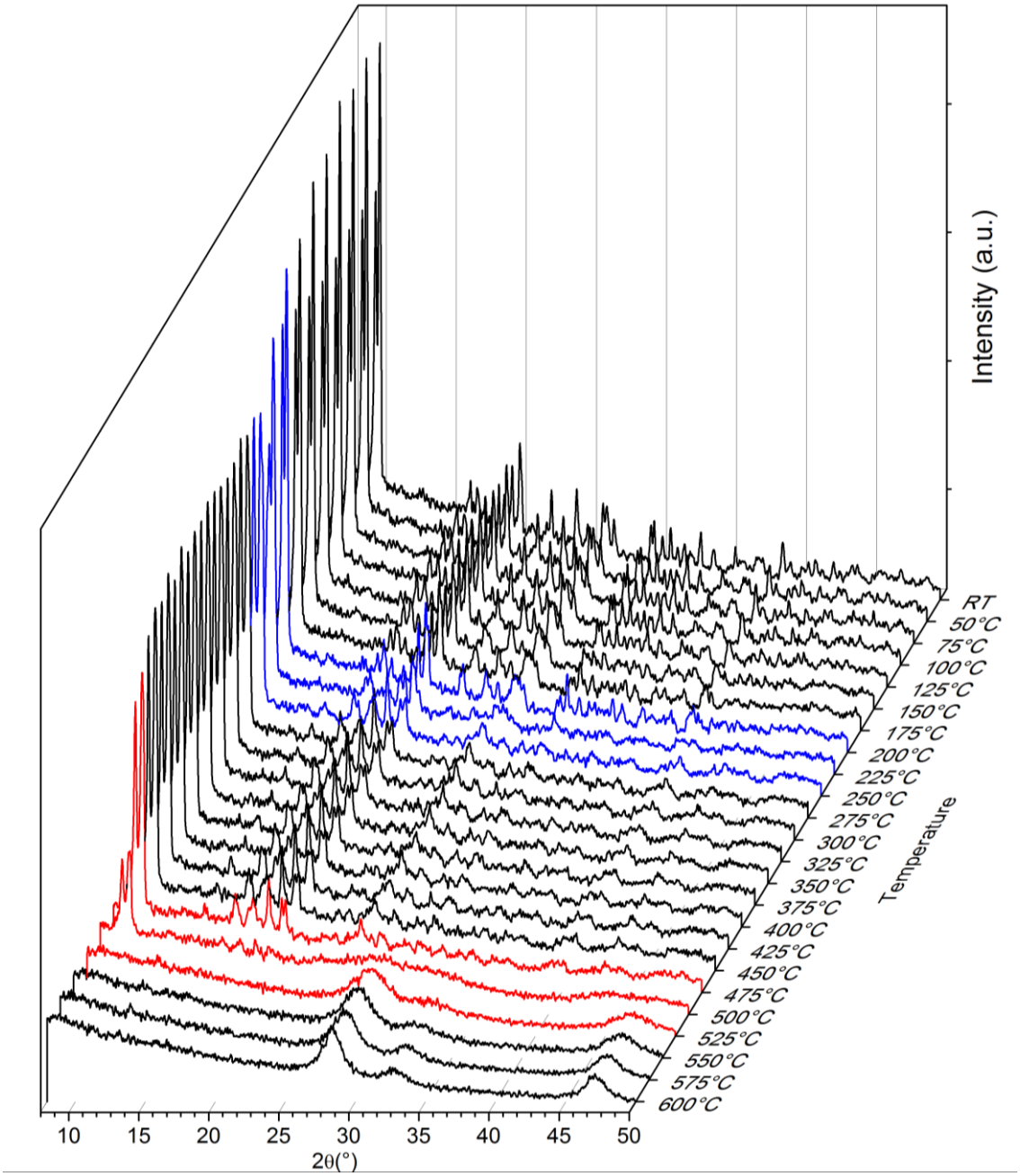

Figure 2. Variable temperature powder X-ray diffraction (VTXRD) recorded in the RT–600 °C range in N_2 flow.

The 3+ oxidation state of Ce in the as-synthesized state and activated at 350 °C material was confirmed by means of XAS spectroscopy, in the XANES region comparison with Ce^{3+} and Ce^{4+} standards. XANES spectra are reported in Figure 3. The 3+ oxidation state was also maintained after activation at 350 °C in the He stream directly in the measurement cell, in agreement with the results reported by the XPS experiments of D'Arras et al. [11].

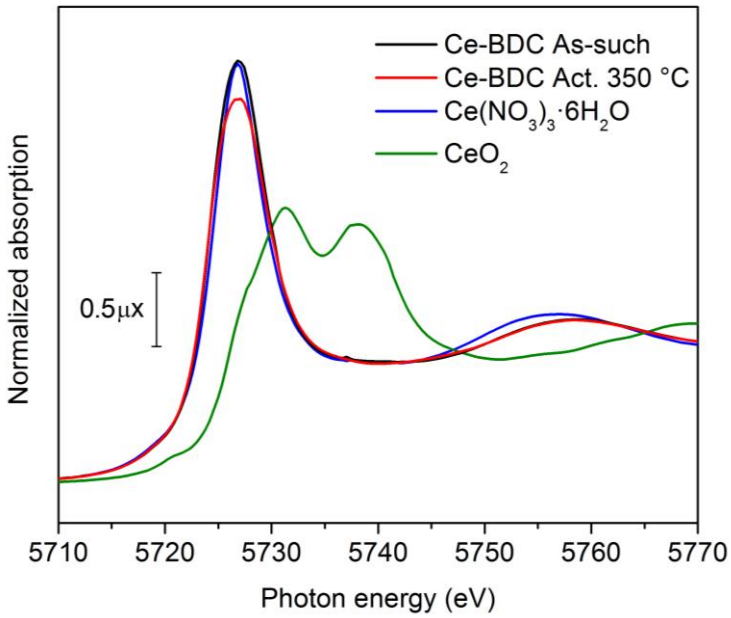

Figure 3. Ce L_3 edge XANES spectra of $Ce_5(BDC)_{7.5}(DMF)_4$ as synthesized and activated at 350 °C, compared with CeO_2 and $Ce(NO_3)_3{\cdot}6H_2O$.

N_2 adsorption volumetric isotherms were measured on the material in order to point out the specific surface area and porosity of the MOF. Thermal treatments were performed in vacuo for 3 h (a longer time in comparison with those ones performed in case of IR or XRD because of the bigger amount of sample) and were made in a consecutive way. From the isotherms reported in Figure 4 it is clear that upon the solvent loss (occurring in the 200–250 °C range) N_2 adsorption grew dramatically, showing microporosity (as the isotherm is a Type I) and higher surface area (more than 200 m^2/g) due to the accessible pores.

BET and Langmuir adsorption models for the surface area were applied; the results are summarized in Table 1. Generally, the reported value can be quite modest for MOF materials, compared with typical MOF surface areas (thousands of m^2/g) [17].

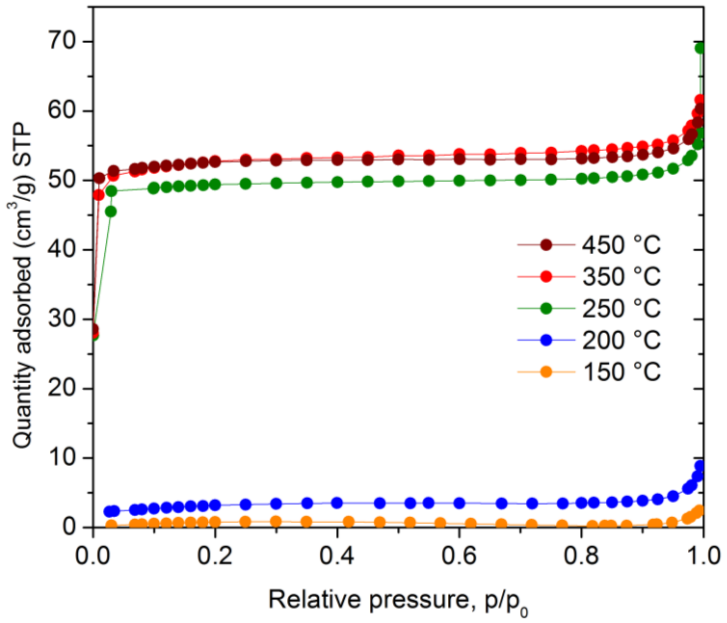

Figure 4. N_2 Adsorption isotherms at −196 °C measured on $Ce_5(BDC)_{7.5}(DMF)_4$. at different activation temperatures (150 °C, 200 °C, 250 °C, 350 °C, 450 °C).

Table 1. BET and Langmuir surface area for $Ce_5(BDC)_{7.5}(DMF)_4$ different temperature treatments.

Treatment	BET Surface Area (m^2/g)	C Value	Langmuir Surface Area (m^2/g)	t-Plot Micropore Volume (cm^3/g)
150 °C-3 h	3.63 ± 0.09	13.6	6.0 ± 0.2	-
200 °C-3 h	11.57 ± 0.06	115.9	16.1 ± 0.2	-
250 °C-3 h	223 ± 2	7110	217.3 ± 0.2	0.072
350 °C-3 h	212 ± 2	6893	232.9 ± 0.5	0.073
450 °C-3 h	216 ± 1	26,545	232 ± 0.4	0.075

As synthesized $Ce_5(BDC)_{7.5}(DMF)_4$ showed the typical mid-IR spectrum for a solvated MOF (see Figure 5). The typical vibrational fingerprints due to DMF solvent molecules mainly inside the pores and to H_2O molecules adsorbed from the atmosphere can be recognized: a broad band centered at 3400 cm^{-1} due to the hydrogen-bonded H_2O molecules and sharp features at frequencies lower than 3000 cm^{-1}, in the range of the aliphatic C–H stretching mode, and a very intense band centered at 1670 cm^{-1}, in the range of the carbonyl stretching mode, due to DMF molecules. Upon progressive outgassing, also by increasing the temperatures, vibrational signals due to DMF and H_2O disappeared and the typical spectrum of a carboxylate-based MOF material was shown: very intense bands in the 1650–1250 cm^{-1} range due to carboxylate stretching modes (both symmetrical and asymmetrical) and sharp features at frequencies higher than 3000 cm^{-1}, in the range of aromatic C–H stretching mode due to BDC^{2-}.

These data support the VTXRD, TGA (see Figure S5), and SSA experiments and therefore we can affirm the material is not destroyed even if activated at 450 °C, maintaining crystallinity and surface area, even if its crystal structure undergoes a phase transition that has not been determined in this study.

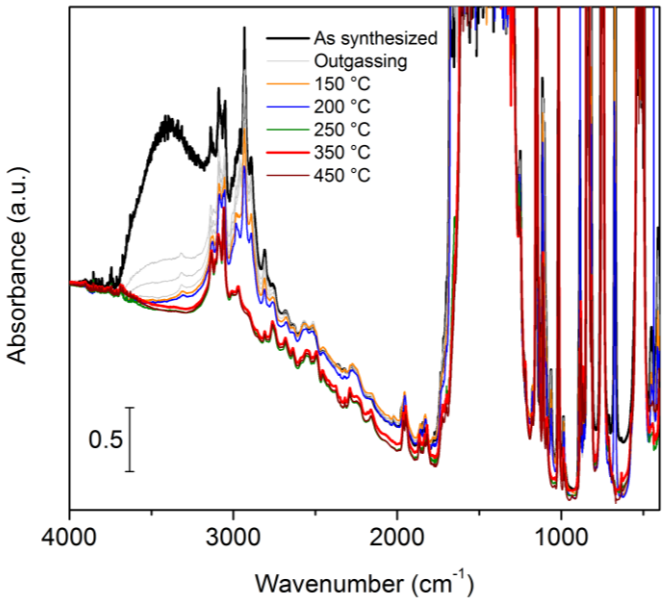

Figure 5. FTIR spectra of $Ce_5(BDC)_{7.5}(DMF)_4$ activated at different temperature in vacuo.

In situ CO adsorption FTIR spectra at −196 °C were recorded on a sample activated at 350 °C for 1 h (see Figure 6). A pressure of 5 mbar of CO was dosed (black spectrum). The lowest frequency peak, at 2131 cm^{-1}, was assigned to the physi-sorbed CO in the pores, as the first one to be desorbed. The other two bands at higher frequencies (2161 cm^{-1} and 2152 cm^{-1}) required more time for complete desorption, and for this reason they can be assigned to CO adsorbed on Lewis acidic sites.

Upon outgassing, the initial activated MOF spectrum was obtained due to the total reversibility of CO adsorption. Because the CO vibrational mode on the MOF open metal sites is intermediate between metals in oxides and metals grafted in different systems [18,19], the doublet can be assigned

to CO adsorbed on Ce^{3+} sites, since CO interacting with Ce^{4+} is expected to give bands at frequencies higher than 2156 cm^{-1} [20,21], in agreement also with XANES results. With the crystal structure of the desolvated material unknown, we can only hypothesize the presence of at least two different Ce^{3+} probed sites [20–22]. Only two out of the five different cerium atoms among the crystallographic asymmetric unit underwent the removal of DMF molecules during activation, however for an in-depth understanding of the desolvation process more investigation is needed. It is of relevance also the overall low intensity of the bands associated with CO adsorption could be due to a low accessibility of the uncoordinated sites. In case of FTIR CO adsorption on MOF-76-Ce [5], two quite intense bands at 2155 cm^{-1} and 2149 cm^{-1}, due, respectively, to the probe interacting with one Ce site and bridged on two close sites, were reported, testifying the completely different local structure of the metal in MOF-76-Ce and in the present $Ce_5(BDC)_{7.5}(DMF)_4$.

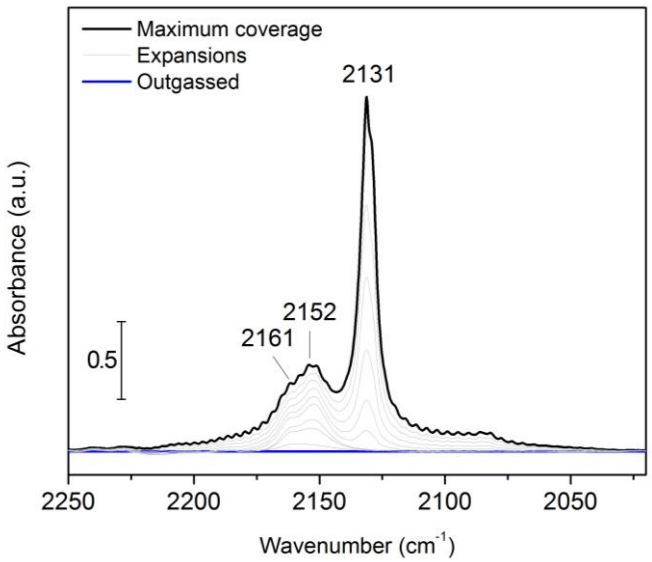

Figure 6. Background-subtracted CO adsorption FTIR spectra at −196 °C on $Ce_5(BDC)_{7.5}(DMF)_4$ activated at 350 °C for 1 h.

CO_2 volumetric isotherms at various activation temperatures are reported in Figure 7. The same powder was heated in vacuo for three hours at the next activation temperature in a consecutive way.

CO_2 uptake showed a clear increase with the activation temperature by reaching a plateau at the 350–450 °C temperature range, as reported in Figure 7 and Table 2.

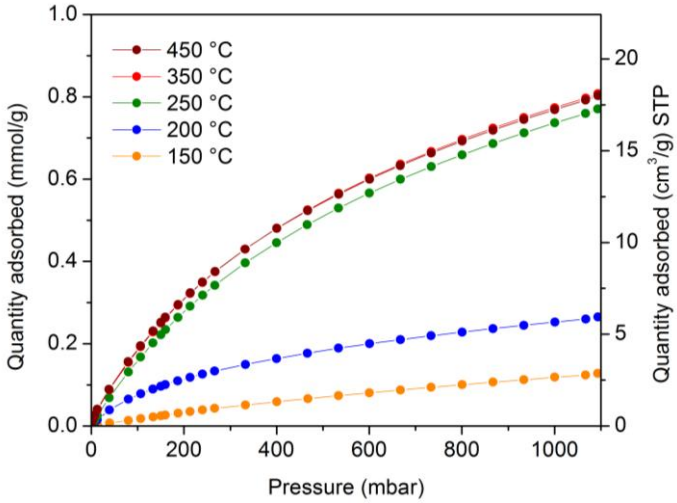

Figure 7. CO_2 Adsorption isotherms at 25 °C on $Ce_5(BDC)_{7.5}(DMF)_4$ at different activation temperatures (150 °C, 200 °C, 250 °C, 350 °C, 450 °C).

Table 2. Summary of CO_2 uptake measurements at 1 bar and 25 °C.

Treatment	CO_2 Uptake at 1 Bar and 25 °C			$n_{ads}/S_{Langmuir}$(1 bar)
	(mol/kg)	(cm^3/g) STP	Weight Percentage	(μmol/m^2)
150 °C-3 h	0.1281	2.87	0.56%	21.4 ± 0.7
200 °C-3 h	0.2728	6.12	1.19%	16.93 ± 0.3
250 °C-3 h	0.7954	17.83	3.38%	3.660 ± 0.004
350 °C-3 h	0.8352	18.72	3.55%	3.586 ± 0.008
450 °C-3 h	0.8301	18.61	3.52%	3.586 ± 0.006

Calorimetric data, reported in Figure 8, were recorded for the adsorption of CO_2 at 30 °C in the 0–90 mbar range. The adsorbed quantity and the heat released by the adsorption as a function of the pressure are plotted, respectively, in Figure 8a,b. Both these curves are nearly Henry-type, as confirmed by the first part of our CO_2 volumetric adsorption isotherms collected with a different instrument at 25 °C (Figure 7). The studied pressure range was too low to observe saturation of the adsorbing sites and the temperature difference of 5 °C between these two experiments was due to technical requirements. The differential heat of adsorption at low coverages was about 32–33 kJ/mol and it is quite typical for the interaction of CO_2 with an open-metal site, as in MOF-76-ds [5], HKUST-1 [23], Mg-MOF-74 [17]. It is worth noting that the differential heat curve (Figure 8c) is characterized by an abrupt diminishing with the adsorbed quantity; this can be ascribed to the overall low number of strongly coordinating sites present in the desolvated material, as highlighted by our CO FTIR experiment (Figure 6). The total reversibility of the adsorption of CO_2 upon outgassing at 30 °C was testified thoroughly by the perfect recovery of the adsorption properties between the primary and secondary adsorption cycles.

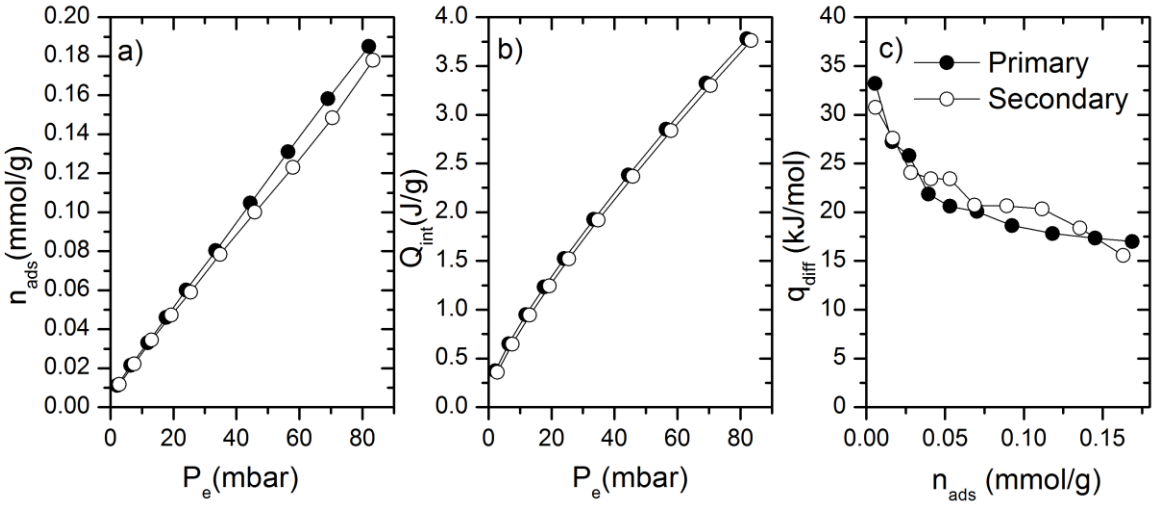

Figure 8. (**a**) Volumetric isotherm (**b**) calorimetric isotherm and (**c**) differential heat distribution of CO_2 adsorption measured at 30 °C on $Ce_5(BDC)_{7.5}(DMF)_4$ activated at 350 °C.

3. Materials and Methods

The variable temperature X-ray diffraction patterns (VTXRD) were collected with an X'Pert PRO MPD diffractometer from PANalytical (Almelo, The Netherlands), working in Bragg–Brentano geometry equipped with a Cu Kα source using about 10 mg of sample. Scattered photons were revealed by an X'celerator linear detector (PANalytical, Almelo, The Netherlands) equipped with a Ni filter to attenuate Kβ. A non-ambient chamber XRK900 from Anton Paar (Graz, Austria) with Be windows was used to collect diffractograms as a function of temperature in a flow of dry N_2 (20 mL/min). The temperature program was set to measure a pattern every 25 °C, waiting 25 min at the target temperature before collecting the data. The temperature was increased at a rate of 2 °C/min.

X-Ray absorption spectra at the Ce L_3 edge (5723 eV) were collected at the BM23 beamline of the European Synchrotron Radiation Facility (ESRF). Data were acquired up to the Ce L_2 edge (6164 eV),

which limited the EXAFS signal down to k ≈ 10 Å^{-1}.The acquisition step was set to 0.3 eV in the near-edge region and Δk = 0.035 Å^{-1} in the EXAFS part of the spectrum. We used three He/N_2-filled ionization chambers as I_0, I_1, and I_2 detectors, placing chromium foil between I_1 and I_2 for energy calibration. XANES and EXAFS data were analyzed by using the Demeter 0.9.20 package. Sample treatment was carried out in an in situ cell under a flow of He (80 mL min^{-1}). During activation, the sample was heated to 350 °C after a ramp heating at 4 °C min^{-1}, to then be cooled to 30 °C.

Adsorption isotherms were collected on an ASAP 2020 apparatus from Micromeritics (Norcross, GA, USA) using a liquid nitrogen bath at −196 °C, albeit CO_2 isotherms were collected filling the same dewar vessel with water at 25 °C. About 150 mg of sample was heated in dynamic vacuum at 350 °C for 3 h prior to measuring the isotherm. Langmuir fit was made in the $0.05 < p/p_0 < 0.2$ range, while the BET analysis was carried out in a very low-pressure region, as prescribed by the so-called Rouquerol rules [24], in order to obtain a positive C value.

FTIR spectra were collected on a Nicolet 6700 from Thermo Scientific (Waltham, MA, USA) equipped with an MCT detector in the 4000–400 cm^{-1} range with a resolution of 2 cm^{-1}. The sample was prepared by pressing a thin self-supporting pellet (10 mg of sample) and using a vacuum line and a jacketed IR cell of local construction capable of cooling down the sample with liquid nitrogen and permitting the dosing of probe molecules (i.e., CO). The experiment was run by activating the pellet in dynamic vacuum at 350 °C for 1 h, then dosing about 15 mbar of CO on the sample to record spectra during cooling to the liquid nitrogen temperature, desorption, and then heating back to RT.

Adsorption heats were measured simultaneously with the adsorption isotherms by means of a C80 Tian-Calvet microcalorimeter from Setaram (Caluire-et-Cuire, France) at a temperature of 30 °C, coupled with a glass vacuum line of local construction. The procedure is thoroughly described in references [25,26], and in this case required thermal activation under dynamic vacuum at 350 °C for 3 h, then an overnight outgassing at 30 °C in the calorimeter before measuring the primary and the secondary adsorption runs in order to determine the non-desorbable (irreversible) fraction.

4. Conclusions

The synthesis of $Ce_5(BDC)_{7.5}(DMF)_4$ was successful, starting from $Ce(NO_3)_3{\cdot}6H_2O$ and H_2BDC in solvothermal conditions in DMF at 140 °C. We obtained the same crystal structure reported by D'Arras et al. [11] using a Ce^{3+} source directly, conversely to the previous contribution. The thermal stability (up to 475 °C in an inert atmosphere) previously observed by D'Arras et al. [11] was confirmed by our VTXRD and TGA measurements. Differently from D'Arras et al. [11] we found a discrete surface area due to microporosity through N_2 adsorption isotherms at −196 °C (about 220 m^2/g) after thermal activation in the 250–450 °C range. XAS confirmed the presence of Ce^{3+} in the material also after desolvation. FTIR spectroscopy confirmed the successful removal of DMF within the pore system at temperatures above 250 °C, and by means of low-temperature CO adsorption evidenced the presence of a Ce^{3+} open metal sites. The interaction of the desolvated material with CO_2 was characterized by volumetric and calorimetric measurements, finding a modest capacity of adsorption (about 3.5 wt % at 1 bar and 25 °C) but a relevant enthalpy (32–33 kJ/mol) for the very first dose, compatible with the presence of open metal sites. This work can open the way to a deep understanding and description of this MOF crystal structure and phase changes upon activation.

Supplementary Materials: The following are available online at www.mdpi.com/2304-6740/8/2/9/s1, Figure S1: Diffractograms of 1, 3, 4, and 6 batches: adopted solvent and metal to ratio (M:L) are reported, Figure S2: Diffractograms of 8, 12, 19 batches: reaction conditions are reported, Figure S3: Diffractograms of batch 19 and the MOF reported by D'Arras et al., Figure S4: SEM images of $Ce_5(BDC)_{7.5}(DMF)_4$ MOF. Part (b) reports a magnification of a portion reported in part (a), Figure S5: TGA in N_2 (solid line) and dry (dash-dotted line) air flow of $Ce_5(BDC)_{7.5}(DMF)_4$ MOF, Figure S6: Magnitude of the Fourier transform of k^2 χ(k) EXAFS signal (phase uncorrected) at different temperatures of $Ce_5(BDC)_{7.5}(DMF)_4$. 2.74 < k < 9.874 Å^{-1} range for the transform is used, Figure S7: Background subtracted CO_2 adsorption FTIR spectra at RT on $Ce_5(BDC)_{7.5}(DMF)_4$ activated 350 °C for 1 h.

Author Contributions: Conceptualization, F.B. and J.E.; Methodology, F.B., J.E., and C.A.; Formal Analysis, C.A.; Investigation, C.A.; Resources, S.B.; Data Curation, C.A.; Writing—Original Draft Preparation, F.B. and C.A.;

Writing—Review and Editing, all authors; Visualization, C.A. and F.B.; Validation, V.C.; Supervision, F.B. and S.B. All authors have read and agreed to the published version of the manuscript.

Funding: This research was funded by The Italian Ministry of Education, University and Research (MIUR), grant number 2017KKP5ZR (PRIN project). The APC was funded by the same institution.

Acknowledgments: Claudia Barolo is acknowledged for the fruitful discussion during the synthetic procedure optimization. The autors thank Jenny G. Vitillo for the help in collecting the adsorption data and Kirill A. Lomachenko for XAS data collection.

Conflicts of Interest: The authors declare no conflict of interest.

References

1. Haxel, G.B.; Hedrick, J.B.; Orris, G.J. *Rare Earth Elements—Critical Resources for High Technology Supporting Sound Management of Our Mineral Resources*; USGS: Reston, VA, USA, 2002.
2. Long, K.R.; Van Gosen, B.S.; Foley, N.K.; Cordier, D. *The Principal Rare Earth Elements Deposits of the United States: A Summary of Domestic Deposits and a Global Perspective*; USGS: Reston, VA, USA, 2012.
3. Montini, T.; Melchionna, M.; Monai, M.; Fornasiero, P. Fundamentals and Catalytic Applications of CeO_2-Based Materials. *Chem. Rev.* **2016**, *116*, 5987–6041.
4. Kašpar, J.; Fornasiero, P.; Graziani, M. Use of CeO_2-based oxides in the three-way catalysis. *Catal. Today* **1999**, *50*, 285–298.
5. Ethiraj, J.; Bonino, F.; Vitillo, J.G.; Lomachenko, K.A.; Lamberti, C.; Reinsch, H.; Lillerud, K.P.; Bordiga, S. Solvent-Driven Gate Opening in MOF-76-Ce: Effect on CO_2 Adsorption. *ChemSusChem* **2016**, *9*, 713–719.
6. Atzori, C.; Lomachenko, K.A.; Øien-ØDegaard, S.; Lamberti, C.; Stock, N.; Barolo, C.; Bonino, F. Disclosing the Properties of a New Ce(III)-Based MOF: $Ce_2(NDC)_3(DMF)_2$. *Cryst. Growth Des.* **2019**, *19*, 787–796.
7. Lammert, M.; Wharmby, M.T.; Smolders, S.; Bueken, B.; Lieb, A.; Lomachenko, K.A.; De Vos, D.; Stock, N. Cerium-based metal organic frameworks with UiO-66 architecture: Synthesis, properties and redox catalytic activity. *Chem. Commun.* **2015**, *51*, 12578–12581.
8. Smolders, S.; Lomachenko, K.A.; Bueken, B.; Struyf, A.; Bugaev, A.L.; Atzori, C.; Stock, N.; Lamberti, C.; Roeffaers, M.B.J.; De Vos, D.E. Unravelling the Redox-catalytic Behavior of Ce^{4+} Metal–Organic Frameworks by X-ray Absorption Spectroscopy. *ChemPhysChem* **2018**, *19*, 373–378.
9. Lammert, M.; Glißmann, C.; Reinsch, H.; Stock, N. Synthesis and Characterization of New Ce(IV)-MOFs Exhibiting Various Framework Topologies. *Cryst. Growth Des.* **2017**, *17*, 1125–1131.
10. Griffin, S.L.; Wilson, C.; Forgan, R.S. Uncovering the structural diversity of Y(III) naphthalene-2,6-dicarboxylate MOFs through coordination modulation. *Front. Chem.* **2019**, *7*, 36.
11. D'Arras, L.; Sassoye, C.; Rozes, L.; Sanchez, C.; Marrot, J.; Marre, S.; Aymonier, C. Fast and continuous processing of a new sub-micronic lanthanide-based metal–organic framework. *New J. Chem.* **2014**, *38*, 1477.
12. Rhauderwiek, T.; Heidenreich, N.; Reinsch, H.; Øien-ØDegaard, S.; Lomachenko, K.A.; Rütt, U.; Soldatov, A.V.; Lillerud, K.P.; Stock, N. Co-Ligand Dependent Formation and Phase Transformation of Four Porphyrin-Based Cerium Metal–Organic Frameworks. *Cryst. Growth Des.* **2017**, *17*, 3462–3474.
13. Lammert, M.; Reinsch, H.; Murray, C.A.; Wharmby, M.T.; Terraschke, H.; Stock, N. Synthesis and structure of Zr(IV)- and Ce(IV)-based CAU-24 with 1,2,4,5-tetrakis(4-carboxyphenyl)benzene. *Dalton Trans.* **2016**, *45*, 18822–18826.
14. Lammert, M.; Glißmann, C.; Stock, N. Tuning the stability of bimetallic Ce(IV)/Zr(IV)-based MOFs with UiO-66 and MOF-808 structures. *Dalton Trans.* **2017**, *46*, 2425–2429.
15. Lomachenko, K.A.; Jacobsen, J.; Bugaev, A.L.; Atzori, C.; Bonino, F.; Bordiga, S.; Stock, N.; Lamberti, C. Exact Stoichiometry of Ce_xZr_{6-x} Cornerstones in Mixed-Metal UiO-66 Metal–Organic Frameworks Revealed by Extended X-ray Absorption Fine Structure Spectroscopy. *J. Am. Chem. Soc.* **2018**, *140*, 17379–17383.
16. Atzori, C. Synthesis and Characterization of a Ce-Based Metal–Organic Framework (MOF). Master's Thesis, Università di Torino, Turin, Italy, 2014.
17. Sumida, K.; Rogow, D.L.; Mason, J.A.; McDonald, T.M.; Bloch, E.D.; Herm, Z.R.; Bae, T.-H.; Long, J.R. Carbon Dioxide Capture in Metal–Organic Frameworks. *Chem. Rev.* **2012**, *112*, 724–781.
18. Chavan, S.; Bonino, F.; Vitillo, J.G.; Groppo, E.; Lamberti, C.; Dietzel, P.D.C.; Zecchina, A.; Bordiga, S. Response of CPO-27-Ni towards CO, N_2 and C_2H_4. *Phys. Chem. Chem. Phys.* **2009**, *11*, 9811–9822.

19. Bordiga, S.; Regli, L.; Bonino, F.; Groppo, E.; Lamberti, C.; Xiao, B.; Wheatley, P.S.; Morris, R.E.; Zecchina, A. Adsorption properties of HKUST-1 toward hydrogen and other small molecules monitored by IR. *Phys. Chem. Chem. Phys.* **2007**, *9*, 2676–2685.
20. Vindigni, F.; Manzoli, M.; Tabakova, T.; Idakiev, V.; Boccuzzi, F.; Chiorino, A. Effect of ceria structural properties on the catalytic activity of Au–CeO_2 catalysts for WGS reaction. *Phys. Chem. Chem. Phys.* **2013**, *15*, 13400.
21. Binet, C.; Daturi, M.; Lavalley, J.C. IR study of polycrystalline ceria properties in oxidised and reduced states. *Catal. Today* **1999**, *50*, 207–225.
22. Chavan, S.M.; Shearer, G.C.; Svelle, S.; Olsbye, U.; Bonino, F.; Ethiraj, J.; Lillerud, K.P.; Bordiga, S. Synthesis and Characterization of Amine-Functionalized Mixed-Ligand Metal–Organic Frameworks of UiO-66 Topology. *Inorg. Chem.* **2014**, *53*, 9509–9515.
23. Grajciar, L.; Bludský, O.; Nachtigall, P. Water adsorption on coordinatively unsaturated sites in CuBTC MOF. *J. Phys. Chem. Lett.* **2010**, *1*, 3354–3359.
24. Thommes, M.; Kaneko, K.; Neimark, A.V.; Olivier, J.P.; Rodriguez-Reinoso, F.; Rouquerol, J.; Sing, K.S.W. Physisorption of gases, with special reference to the evaluation of surface area and pore size distribution (IUPAC Technical Report). *Pure Appl. Chem.* **2015**, *87*, 1051–1069.
25. Auroux, A. *Calorimetry and Thermal Methods in Catalysis*; Auroux, A., Ed.; Springer Series in Materials Science; Springer: Berlin/Heidelberg, Germany, 2013; Volume 154, ISBN 978-3-642-11953-8.
26. Bolis, V.; Maggiorini, S.; Meda, L.; D'Acapito, F.; Turnes Palomino, G.; Bordiga, S.; Lamberti, C. X-ray photoelectron spectroscopy and X-ray absorption near edge structure study of copper sites hosted at the internal surface of ZSM-5 zeolite: A comparison with quantitative and energetic data on the CO and NH_3 adsorption. *J. Chem. Phys.* **2000**, *113*, 9248–9261.

© 2020 by the authors. Licensee MDPI, Basel, Switzerland. This article is an open access article distributed under the terms and conditions of the Creative Commons Attribution (CC BY) license (http://creativecommons.org/licenses/by/4.0/).